We are IntechOpen, the world's leading publisher of Open Access books Built by scientists, for scientists

6,900
Open access books available

185,000
International authors and editors

200M
Downloads

Our authors are among the

154
Countries delivered to

TOP 1%
most cited scientists

12.2%
Contributors from top 500 universities



WEB OF SCIENCE™

Selection of our books indexed in the Book Citation Index in Web of Science™ Core Collection (BKCI)

Interested in publishing with us?
Contact book.department@intechopen.com

Numbers displayed above are based on latest data collected.
For more information visit www.intechopen.com



Chapter 3

Tsunami Wave Propagation

Alexey Androsov, Sven Harig, Annika Fuchs, Antonia Immerz, Natalja Rakowsky, Wolfgang Hiller and Sergey Danilov

Additional information is available at the end of the chapter

http://dx.doi.org/10.5772/51340

1. Introduction

Tsunami hazard is connected with loss of human life, flooding of coastal structures, destruction of berthing designs, infrastructures of coastal water areas.

In support of the Tsunami Early Warning System for the Indian Ocean, a finite element model TsunAWI for simulations of wave propagation has been developed. It is part of German Indonesian Tsunami Early Warning System (GITEWS) (www.gitews.de) serving to predict arrival times and expected wave heights. TsunAWI is based on an unstructured grid approach employing finite elements to solve the governing equations.

Finite-element methods are widely used in studies of wave generation and propagation in different fields of fluid dynamics. They are often employed to simulate propagation of long waves such as ocean tides and tsunamis in the ocean in the framework of shallow-water equations [1–3]. The main reason to prefer FE modelling is that the solution is computed over a mesh that can be adapted to cover basins with complex geometries characterized by irregular bottom topography and coastlines.

The purpose of this work is to describe a complex system of tsunami warning, based on the numerical modelling of tsunami events in Indian Ocean. The complexity of the problem stems from insufficient information about the sources generating tsunami, real bottom morphometry and extremely short warning time. In addition, some physical processes, such as interaction of tsunami waves with long tidal waves or nonhydrostatic effects, commonly neglected in models of tsunami wave propagation, may lead to substantial corrections.

Our work, therefore, addresses the influence of tidal dynamics on tsunami wave propagation in coastal areas. A tsunami wave is much shorter than tidal waves which explain why tidal waves are usually ignored in tsunami modelling. There are three approaches to account for the interaction between tsunami waves and tides. The first one presumes that the wave propagation is linear, so that tides reduce or augment (depending on their phase) the amplitude of arriving waves [4]. In this case, having simulated tidal patterns in advance, it

INTECH
open science | open minds

©2013 Androsov et al., licensee InTech. This is an open access chapter distributed under the terms of the Creative Commons Attribution License (http://creativecommons.org/licenses/by/3.0), which permits unrestricted use, distribution, and reproduction in any medium, provided the original work is properly cited.

would be possible to predict arriving waves as a simple superposition of signals. The second approach assumes that the interaction has a nonlinear character caused by changes in the fluid layer thickness in the shallow area [5]. Finally, the third approach suggests that the main effect is due to nonlinear interactions between tidal and tsunami velocities [6]. The studies performed thus far are of theoretical character and do not involve practical examples.

As a tsunami wave arrives in coastal regions with rough bathymetry, the nonhydrostatic part of pressure, neglected in the standard hydrostatic configuration of TsunAWI, gains in importance. The account for nonhydrostatic effects corrects the wave propagation speed. The impact of nonhydrostatic effects is investigated using the standard benchmark problem of a solitary wave runup on a plane beach [7].

The organization of present work is as follows. Section 2 introduces the basic equations, the numerical implementation of the model and the mesh generation algorithm. Its final part presents the nonhydrostatic pressure correction algorithm. Section 3 describes the architecture of the Tsunami Early Warning System. In section 4, the system is applied to simulate some realistic scenario of tsunami wave propagation in the Indian Ocean. Section 5 deals with tidal-tsunami interactions whereas section 6 illustrates manifestations of nonhydrostatic effects. Section 7 contains the conclusions of the work.

2. Description of the model

2.1. Boundary-value problem in Cartesian coordinates

In the domain $\widetilde{\Omega} = \{(x, y) \in \Omega, 0 \leq t \leq T\}$, where Ω is a plane domain with boundary $\partial\Omega$, we consider the vertically averaged equations of motion and continuity

$$\mathbf{v}_t + (\mathbf{v} \cdot \nabla)\mathbf{v} + g\nabla\zeta = \Phi \equiv f\mathbf{k} \times \mathbf{v} - rH^{-1}\mathbf{v}|\mathbf{v}| + H^{-1}\nabla(K_h H \nabla \mathbf{v}), \tag{1}$$

$$\zeta_t + \nabla \cdot (H\mathbf{v}) = 0, \tag{2}$$

where $\mathbf{v} = (u, v)$ is the horizontal velocity vector, $H = h + \zeta$ is the total water depth, $H > 0$, h is the unperturbed water depth, and ζ is the surface elevation, $\nabla = (\partial/\partial x, \partial/\partial y)$ is the gradient operator, f the Coriolis parameter, $\mathbf{k}$ is the unit vector in the vertical direction, r is the bottom friction coefficient, and K_h is the eddy viscosity coefficient. The set of (1) and (2) is known as the rotating shallow water equations.
On the solid part of the boundary, $\partial\Omega_1$, and on its open part, $\partial\Omega_2$, we impose the following boundary conditions

$$v_n|_{\partial\Omega_1} = 0, \quad \Gamma(\mathbf{v}, \zeta)|_{\partial\Omega_2} = \Theta_1, \tag{3}$$

where v_n is the velocity normal to $\partial\Omega_1$, Γ is the operator of the boundary conditions and Θ_1 is a vector-function determined by the boundary regime and different for inflow and outflow [8]. In practice, when the full information on the open boundary is unavailable, in place of the second condition (3) one commonly imposes the boundary condition on the elevation $\zeta|_{\partial\Omega_2} = \psi(x, y, t)$ or the radiation boundary condition $\mathbf{v}_n = \mathbf{v} \cdot \mathbf{n} = \sqrt{g/H}\zeta$. The latter provides free linear wave passage through the open boundary (when the Coriolis acceleration plays a small role). Here $\mathbf{n}$ is the outer unit normal to $\partial\Omega_2$. The accuracy of the reduced boundary-value formulation with only the sea level assigned at the open boundary, was analyzed in [9]. The

problem (1)-(3) for the combination $\mathbf{u} = (\mathbf{v}, \zeta)$ is solved for given initial conditions: $\mathbf{u}|_{t=0} = \mathbf{u}^0$.

The equation of energy for set (1) and (2) has the form

$$\frac{\partial E}{\partial t} + \nabla \cdot \left[H \left(g\zeta + \frac{1}{2} |\mathbf{v}|^2 \right) \mathbf{v} \right] = -r |\mathbf{v}|^{3/2} + \mathbf{v} \cdot \nabla (K_h H \nabla \mathbf{v}) \tag{4}$$

where

$$E = \frac{1}{2} \left(H |\mathbf{v}|^2 + g\zeta^2 \right) \tag{5}$$

is the total energy per unit area.

2.2. Method

The finite element spatial discretization is based on the approach by Hanert et al. [10] with some modifications like added viscous and bottom friction terms, corrected momentum advection terms, radiation boundary condition and nodal lumping of mass matrix in the continuity equation. The basic principles of discretization follow the paper of [10] and are not repeated here.

Simulation of tsunami wave propagation benefits from using an explicit time discretization. Indeed, numerical accuracy requires relatively small time steps, which reduces the main advantage of implicit schemes. Furthermore, modelling the inundation processes usually requires very high spatial resolution in coastal regions (up to some tens of meters) and consequently large number of nodes, drastically increasing necessary computational resources in case of implicit temporal discretization.
The leap-frog discretization was chosen as a simple and easy to implement method. We rewrite eqs. (1) and (2) in time discrete form,

$$\frac{\mathbf{v}^{n+1} - \mathbf{v}^{n-1}}{2\Delta t} + fk \times \mathbf{v}^n + g\nabla\zeta^n + \frac{r}{H^n} |\mathbf{v}^n| \mathbf{v}^{n+1} - \nabla K_h \nabla \mathbf{v}^{n-1} + (\mathbf{v}^n \nabla)\mathbf{v}^n = 0, \tag{6}$$

$$\frac{\zeta^{n+1} - \zeta^{n-1}}{2\Delta t} + \nabla \cdot (H^n \mathbf{v}^n) = 0. \tag{7}$$

Here Δt is the time step length and n the time index. The leap-frog three-time-level scheme provides second-order accuracy and is neutral within the stability range. This scheme however has a numerical mode which is removed by the standard filtering procedure. Notice that friction and viscosity contributions deviate from the usual leap-frog method.

2.3. Momentum advection scheme

Because of the discontinued character of velocity representation, special care is required with respect to the implementation of momentum advection. Earlier experiments with $P_1^{NC} - P_1$ code revealed problems with spatial noise and instability of momentum advection when the discretization is used in the form described in [10]. A modified implementation without upwinding terms was found to work well, yet when paired with rather high viscous dissipation for removing small-scale noise in the velocity field. In addition, the

implementation of the momentum advection for P_1^{NC} velocities involves cycling over edges in the numerical code, in addition to cycling over elements to assemble the elemental (regular) contributions. This reduces numerical efficiency. This lead us to a simpler approach, which provides some smoothing of the velocity field while removing edge contributions.
According to this approach, prior to calculating the advection term in the momentum equation we project the velocity from the P_1^{NC} to the P_1 space in order to smooth it. To make this projection numerically efficient, nodal quadrature (lumped mass matrix) is employed. The projected velocity is then used to estimate the advection term. Finally we proceed as usual by multiplying the result with a P_1^{NC} basis function and integrating over the domain [11]. This results in a very stable behaviour.

2.4. Other implementation details

2.4.1. Wetting and drying, viscosity

For modelling wetting and drying we use a moving boundary technique which utilizes linear least square extrapolation through the wet-dry boundary and into the dry region. We apply "dry node concept" developed in [12] The idea of this concept is to exclude dry nodes from the solution and then to extrapolate elevation to the dry nodes from their wet neighbours. Because the scheme is neutrally stable it demands horizontal viscosity in places of large gradients of the solution. The coefficient of horizontal viscosity is determined by a Smagorinsky parameterization [13].

2.4.2. Code parallelization

Since a large number of scenarios has to be calculated, code optimization and parallelization is crucial. The operational version of TsunAWI is parallelized employing OpenMP. It is therefore limited to shared memory platforms. The parallelization is implemented by defining parallel regions in the numerically most demanding parts of the code and splitting up the corresponding loops, thus sharing the load to the CPUs involved. The remaining part of the code stays serial. The implementation in this ideology needs therefore smaller changes than a full parallel implementation based on MPI, and proves to be numerically efficient.

2.4.3. Mesh generation

The quality of the triangulation of the model domain is crucial for the model results. The meshes used in the following studies were generated by a mesh generator based on the freely available software Triangle by Jonathan Shewchuk [14]. Starting from a model domain defined within a topography/bathymetry data set (in our case GEBCO 30″) Triangle is used to generate a mesh based on a refinement rule depending on the water depth and prescribed by the corresponding wave phase velocity and the CFL criterion. The triangulation will be refined until the edges in all triangles fulfill the criterion

$$\Delta x \leq \min\{c\sqrt{gh}, c_g \frac{h}{\nabla h}\} \tag{8}$$

Since the Triangle output is not yet smooth enough for numerical experiments several iterations of smoothing are applied. Smoothing steps consist of edge swapping, torsion

smoothing and linear smoothing. Torsion smoothing tries to equal out angles around each node, linear smoothing acts on the distance between nodes. These strategies are described in [15].

2.5. Nonhydrostatic approach

2.5.1. Limitations of the shallow water model

The shallow water equations are derived on the assumption that the horizontal motion of the fluid dominates over the vertical one. Using the wave length λ and the reference water depth h as characteristical values of horizontal and vertical motion the ratio

$$\delta := \frac{h}{\lambda} \ll 1, \tag{9}$$

must be fulfilled. In this case, terms containing the vertical component of velocity are very small compared with others and a model reduced to the two horizontal dimensions still provides a good approximation of the three-dimensional flow transport. In the course of neglecting the impact of vertical motion, the hydrostatic approximation is approved: The pressure term is limited to static pressure $p_0 = \rho g(\zeta - z)$, as dynamic pressure forces are mainly induced by vertical elevation. With regard to tsunami propagation, condition (9) is satisfied in deep ocean, as the wave length accounts for hundreds of kilometers. When the tsunami reaches coastal regions, the wave length decreases rapidly and the ratio δ as defined above may become less strict, especially in the presence of horizontal inhomogeneities. Waves become dispersive in this limit. They cannot be represented by the standard shallow water equations since in a hydrostatic model the phase velocity $c \approx \sqrt{gh}$ of a wave packet is not affected by the wave length. A more accurate model may be required near the shore. We are seeking how to improve TsunAWI so that the nonhydrostatic effects can be taken into account if required.

2.5.2. The nonhydrostatic approach

In search of approach that corrects the given one, it is useful to look at terms neglected so far. The deviation from the hydrostatic approximation to the real pressure

$$p' = p - p_0 \tag{10}$$

is of particular interest and serves as a starting point. Returning to the momentum equation in vertical direction and considering the missing nonhydrostatic pressure term in (1), the depth-averaged momentum equations result in

$$\partial_t \mathbf{v} + (\mathbf{v} \cdot \nabla)\mathbf{v} + g\nabla\zeta + \frac{1}{\rho H}\int_{-h}^{\zeta} \nabla p' \mathrm{d}z = \Phi \tag{11}$$

$$\partial_t w + (\mathbf{v} \cdot \nabla)w \qquad + \frac{1}{\rho H}\int_{-h}^{\zeta} \partial_z p' \mathrm{d}z = 0 \tag{12}$$

in which w describes the depth-averaged vertical velocity component. Both additional unknowns w and p' are simplified by assuming linear behavior of non-averaged fields in

vertical direction. The values at surface and bottom are partly given by the boundary conditions: the kinematic boundary conditions determine the vertical velocities w_ζ and w_{-h} as

$$w_\zeta = \partial_t \zeta + \mathbf{v} \cdot \nabla \zeta, \tag{13}$$

$$w_{-h} = \quad - \mathbf{v} \cdot \nabla h. \tag{14}$$

At the surface, the boundary condition for pressure enforces the nonhydrostatic part of pressure to vanish, just like the hydrostatic counterpart. Hence, p' depends only on nonhydrostatic bottom pressure $q := p'_{-h}$.

2.5.3. Discretization

For solving equations (11) and (12) a two-step procedure is applied, as suggested in [16] in the framework of finite-difference model, used in [17] for wave breaking and run-up issues and realized in a Finite Element/Finite Volume context by [18]. Firstly, the hydrostatic shallow water equations (1), (2) are stepped forward as before, just as the hydrostatic variant of equation (12) with $p' \equiv 0$. The additional unknowns q and w are introduced as vectors containing the values at the nodes of the triangulation in the same way as the sea surface elevation ζ. In a second step the resulting velocity vector $(\tilde{\mathbf{v}}, \tilde{w})$ is corrected by

$$\mathbf{v}^{n+1} = \tilde{\mathbf{v}}^{n+1} + \frac{2\Delta t}{\rho} \left(\nabla \frac{q^{n+1}}{2} - \frac{q^{n+1}}{2} \frac{\nabla(\zeta^n - h)}{H^n} \right), \tag{15}$$

$$w^{n+1} = \tilde{w}^{n+1} + \frac{2\Delta t}{\rho} \frac{q^{n+1}}{H^n}, \tag{16}$$

in which the correction terms depending on q^{n+1} are nothing else but the calculated integral terms of (11) and (12). The factor $2\Delta t$ arises from using the leapfrog time-stepping scheme. This correction is performed at the end of each time step. However, the nonhydrostatic part of bottom pressure q^{n+1} must be estimated before. While p_0 can be calculated explicitly, the computation of q is performed in an implicit manner. By including the equations (15) and (16) in the depth-integrated continuity equation

$$\int_{-h}^{\zeta} \nabla \cdot \mathbf{v} + \partial_z w \; \mathrm{d}z = 0, \tag{17}$$

the nonhydrostatic bottom pressure can be determined. Because of finite-element discretization, equation (17) reduces to a system of linear equations with a large sparse matrix whose entries vary with time step. As concerns the CPU time, computing q proves to be rather expensive compared to the time required by the shallow water model.

3. The German-Indonesian Tsunami Early Warning System GITEWS

The German-Indonesian Tsunami Early Warning System GITEWS was founded after the devastating Indian Ocean Tsunami 2004 as a joint project of German research institutes leaded by GFZ and Indonesian institutes and authorities. In 2005, Indonesia and Germany

agreed in a joint declaration to develop a warning system coordinated by the UNESCO Intergovernmental Oceanographic Commission. The system was inaugurated in 2008 and evaluated in 2010 by an international commission including the heads of the four operating worldwide tsunami warning centers.

3.1. Architecture of the Indonesian TEWS

The Indonesian warning systems meets the challenge of near field warning with extremely short warning time. As tsunamigenic earthquakes originate close to the shore, the time between a seismic event and the issue of a warning is limited to just a few minutes. The TEWS therefore relies on a repository of tsunami scenarios TSR precomputed with the tsunami model TsunAWI, see section 3.3. Figure 1 shows a schematic overview of the components of

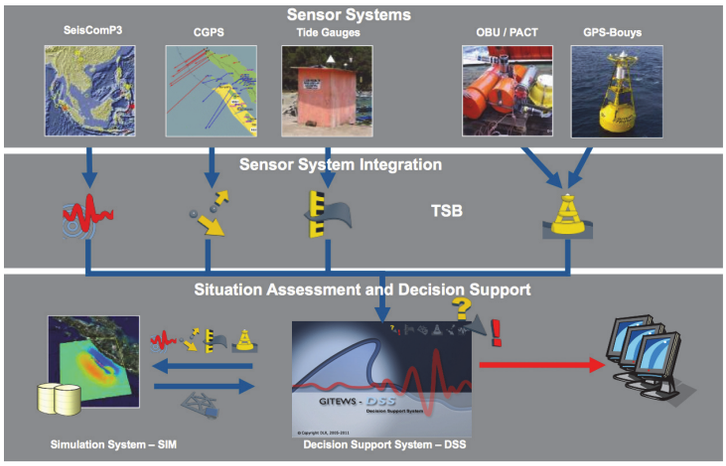


Figure 1. Schematic overview of the early warning process. In case of an earthquake, all available sensor data are gathered by the Decision Support System DSS via the Tsunami Service Bus TSB and sent to the Simulation System SIM. A set of scenarios fitting to the sensor data are delivered and aggregated to an overall perspective.

the TEWS. Data of various sensors, such as the seismic data analyzed by SeisComp, GPS sensors as well as data from tide gauges and buoys is collected via the Tsunami Service Bus TSB [19], and distributed to the Decision Support System DSS [20], which triggers the Simulation System SIM (see section 3.2) with the available sensor data. Based on this data, the SIM delivers a set of best matching scenarios. The DSS performs a worst case aggregation over these scenarios and visualizes expected wave heights and arrival times for the Indonesian coasts. The system is installed at the warning center in Jakarta/Indonesia and assists the Chief Officer on Duty in assessing the potential tsunami risk. He then disseminates warnings to governmental institutions, local disaster management, action forces and media.

3.2. Simulation System (SIM)

In the following the SIM with its components and the algorithm for selecting the best fitting scenarios to an earthquake event shall be introduced in a nutshell. A more detailed overview of the SIM is given in [21], though referring to a prior version of the selection algorithm.

The SIM is written as a Java web application offering web processing WPS and web notification services WNS conforming to the open GIS consortium OGC standard. It is

accessible via HTTP-Requests where request and response details are transferred to and from the SIM in XML format.

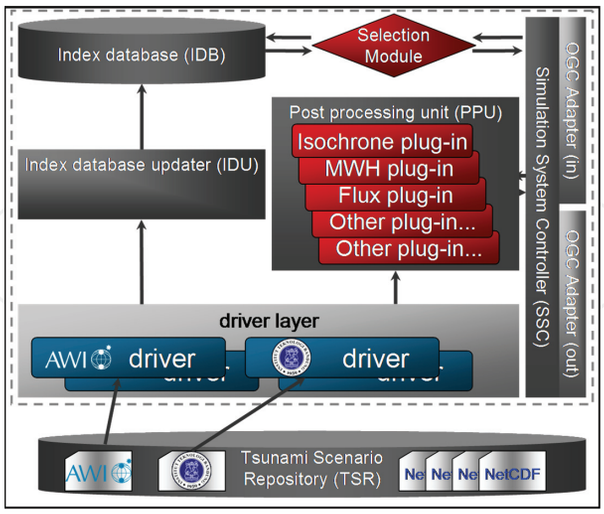


Figure 2. Overview of the SIM software components. Main components are the controller, responsible for overall coordination of processes, the Index Database IDB with data products from the TSR for fast access in case of an event, Postprocessing Unit for extraction of these data products from scenarios, the selection module determining best fitting scenarios for given sensor data, and the OGC-adapter as communication interface.

3.2.1. SIM components

A graphical overview of the software components is given in figure 2.

- Index Database IDB: As mentioned in section 3.1, warning time is crucial for the region of the Sunda Arc. To ensure a response time of the SIM of less than 10 s, significant data products are extracted in advance from each scenario contained in the pre-calculated scenario repository TSR. The IDB contains maximum sea surface height (mwh) and arrivaltimes at coastal forecast zones, isolines of mwh, isochrones, sea surface height time series at tide gauge and buoy locations, and GPS displacement values at GPS station locations.
- Index Database Updater: This component is used to store extracted data products in the index database.
- Postprocessing Unit PPU: The data products are extracted by the post processing plugins compounded in the PPU. The plugins are written in C to employ fast mathematical calculation routines. There task is to extract the information stored in the IDB and to generate SHP-files for visualizing the wave propagation in the DSS. Furthermore, the simulated inundation can be extracted as SHP-files, which are a basis for a priori risk assessment and hazard maps.
- Driver Layer: The driver layer separates the scenario data format from the internal representation of data in the SIM and thus allows to integrate scenarios from different origins and in different formats. One driver per scenario type acts as a translator between scenario data format and the data structure used in the SIM. At the time being, only scenarios calculated with TsunAWI are addressed.

- Scenario Selection Module: The component responsible for the identification of the best fitting scenarios to an earthquake event is described in section 3.2.2.
- Tsunami Scenario Repository TSR: It contains all pre calculated scenarios and is described in more detail in section 3.3

3.2.2. Selection algorithm

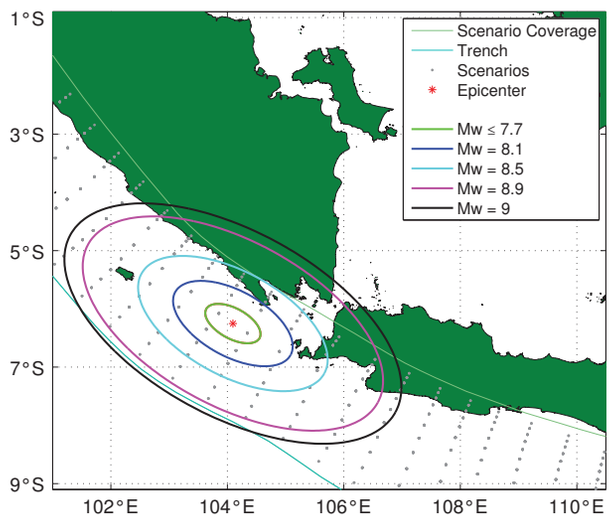


Figure 3. Visualization of the seismic uncertainty ellipse with different size depending on the observed magnitude.

The selection algorithm uses a multi sensor approach combining the different available sensor types to acquire a set of best matching scenarios to an earthquake event. By basing the selection on different sensor data types, uncertainties resulting from inaccurate measurements and errors in the tsunami model are reduced.

In the selection algorithm as described in [21], the different sensor types and even individual sensor stations could be weighted so to factor their individual estimated uncertainty. Initially, the so called matching values generated for each sensor type for a scenario were accumulated in an overall weighted sum of matching values defining a measure of suitability to the current event.

The experiences with real sensor data in the GITEWS project showed that each sensor group has to be regarded separately with its characteristics in mind. The weighted sum over all matching values is therefore replaced by a stepped approach starting with seismic data delivering the most robust values, followed by CGPS data.

The algorithm is specialized for the Sunda Arc taking into advantage that the rupture is often oriented along the trench. The preselection of scenarios based on seismic data is performed by calculating an elliptic area around the measured epicenter within which the selected scenarios lie (figure 3). The dimension of the ellipse depends on the measured magnitude M_W, the long ellipse-axis is given by

$$r_L = 10^{0.5-[M_W+0.3]-1.8}\text{km}.$$

To ensure that at least one scenario is covered, for small magnitudes $\tilde{r}_L = 180$km is chosen. The orientation of the ellipse is derived from the orientation of the trench between the two coordinates found by going $r_L/2$ up an down the trench from the nearest point to the epicenter on the trench.

The second important sensor data class in GITEWS are CGPS dislocation vectors. The sensor data is reliable, and the measurement arrives at the DSS fast, thus allowing for a better estimate of the tsunami hazard in the first few minutes after the earthquake. For each sensor and each scenario (that remains after preselection by the seismic sensor data) the length of the measured and the corresponding scenario dislocation vector are compared. Scenarios for which a defined minimum number of similar GPS values is reached are taken into account for the final set of best fitting scenarios.

If several scenarios are chosen for one epicenter, only those with the largest magnitude within the uncertainty range $[M_w - 0.5, M_w + 0.3]$ is kept in the list, because in DSS processing, a worst case aggregation over all scenarios is performed. For each coastal forecast zone, the shortest arrival time is taken from all scenarios in the list, and the highest maximum wave height. The scenarios with lower magnitudes will not account for this aggregation, hence skipping them reduces the amount of data to be processed without changing the result.

3.3. The Tsunami Scenario Repository

As of March 2012, the GITEWS Tsunami Scenario Repository TSR contains 3470 scenarios for prototypic ruptures (RuptGen2.1 [22]) with magnitudes in the range of Mw=7.2,7.4,...,9.0 on 528 different epicenters, see figure 4. These scenarios for prototypic ruptures in the Sunda

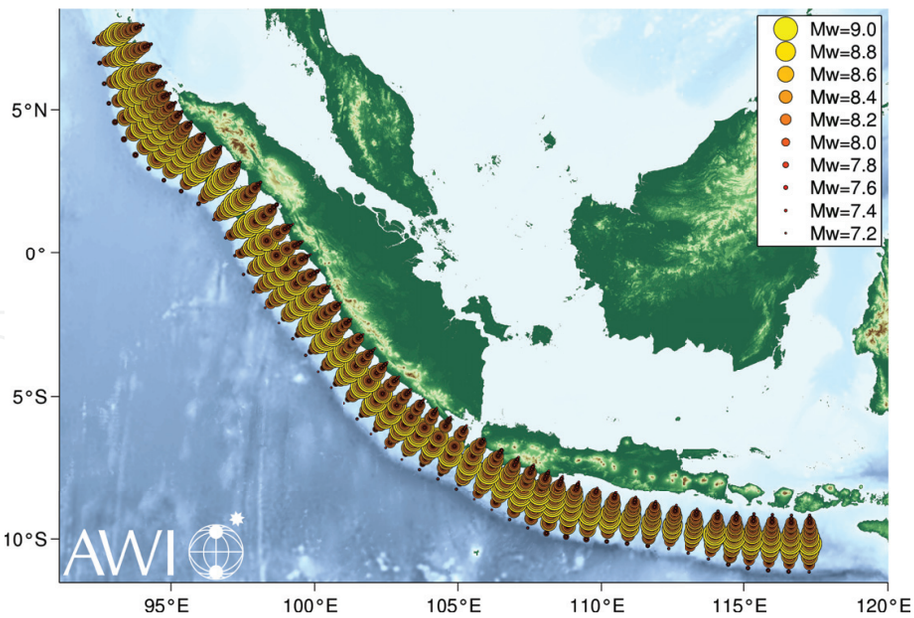


Figure 4. Tsunami scenario repository for GITEWS. Each circle symbolises a scenario with center at the given position. Scenarios for up to ten different magnitudes Mw= 7.2, 7.4, ..., 9.0 are calculated at each of the 528 positions, resulting in 3470 scenarios in total.

Arc are used in the warning situation as well as for a priori risk analysis and hazard maps. The quality of the scenarios, being crucial for both tasks, relies strongly on the numerical

implementation of the governing physical equations and on an accurate representation of the bathymetry and topography especially in coastal regions. Therefore, GITEWS included the development and concise validation of the tsunami model TsunAWI, described in detail in section 4.

For the TSR, TsunAWI operates on a grid with the resolution changing seamlessly between 14 km in deep sea, 150 m at the coast and down to 50 m in regions of special interest, e.g., densely populated areas and at tide gauges. The run-up scheme provides a realistic approximation of the inundation hazard. The dense net of scenarios allows to evaluate the

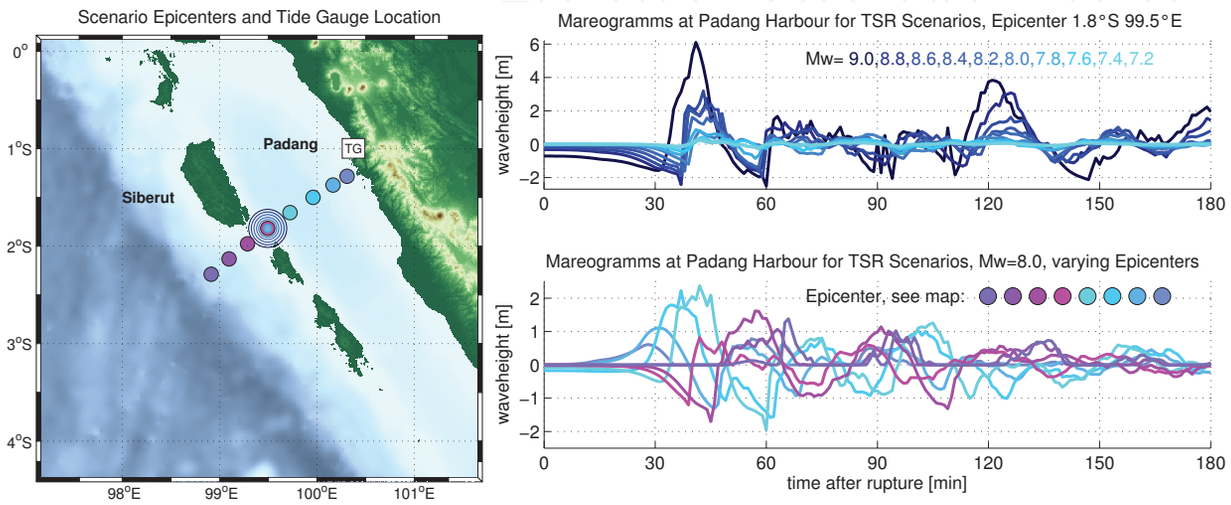


Figure 5. Influence of the magnitude Mw and of the source location on the strength of a tsunami: Mareograms at Padang Harbor for TSR-scenarios originating at the same epicenter with different magnitude (above) and with equal magnitude, but different origin (below).

effect of small changes in epicenter and magnitude as illustrated in figure 5 for artificial mareograms for the harbour of Padang, Sumatra. The logarithmic energy scale of the magnitude is clearly illustrated by the upper mareogram. The lower graph shows more complex features due to varying epicenters on a line perpendicular to the trench. While the magnitude is fixed to Mw=8.0 in this example, the tsunamis originating closest to the coast have the lowest impact. On the one hand, this is due to the initial conditions generated by RuptGen which assumes a source depth of 0 km at the trench increasing up to 100 km under the main islands. A second factor determining the strength of the tsunami is the height of the water column at the origin, and this of course is small in coastal regions.

Epicenters southwest off the coast yield increasing wave heights in Padang, until the Mentawai islands are reached. The pink epicenter marks a turning point where the corresponding tsunami is no longer trapped in reflections between Sumatra and the islands, relieving the situation for Padang.

4. Tsunami modeling with finite elements: applications

TsunAWI is still under development and therefore the performance and model results must be constantly evaluated to ensure a consistent and stable code. Validation needs to be performed on several levels, among these are:

- Consistency / convergence,
- Benchmarks in idealized settings with well defined results,
- Comparisons in real cases with measured data.

This section deals mostly with the last case, section 6 includes some cases with idealized bathymetry and compares hydrostatic and non hydrostatic results.

4.1. Indian Ocean tsunami in December 2004

For the tsunami generated by the great Sumatra-Andaman earthquake on 26 December 2004, a large amount of data is available. In this section model comparisons with observations from satellite altimetry, tide gauge records, and field surveys are discussed. The mesh (figure 6) employed in this study has been generated to deal with all the stages in the propagation of the tsunami. All of the Indian Ocean is covered, the resolution in the deep ocean is about 15 km. In the Aceh region in the Northern tip of Sumatra, where inundation results of the model are compared to field measurements, the mesh size reaches down to 40 m. The results in this section are closely related to the studies published in [23] where additional information can be found.

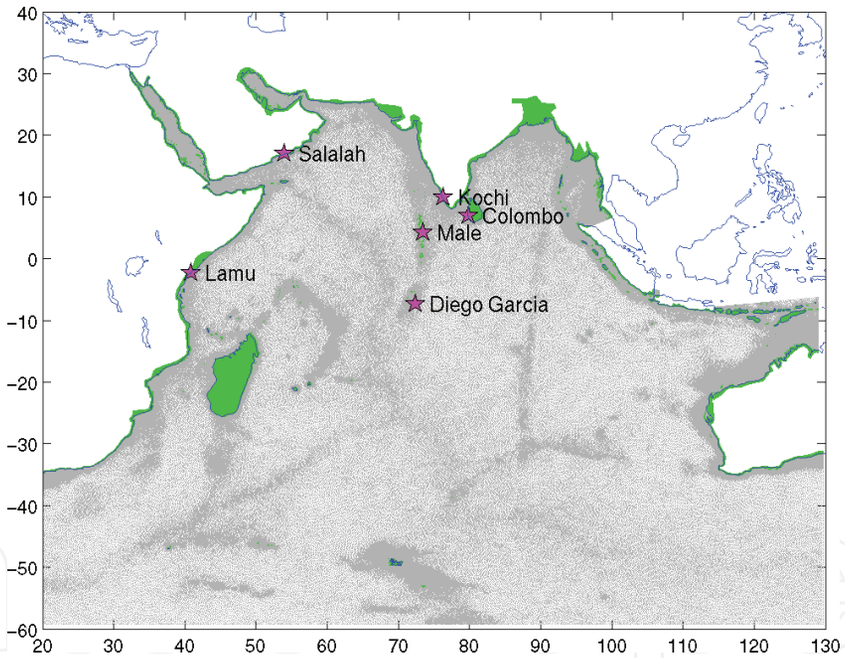


Figure 6. Mesh density in the model domain. The green areas are land nodes contained in the mesh which are initially dry. The resolution ranges from 15 km in the deep ocean to 40 m in the Northern tip of Sumatra.

4.1.1. Available topography and bathymetry data

Topography and bathymetry in the following experiments are based on several data sources. The GEBCO data set [24] is globally available at 30 arc seconds resolution and is used in all meshes as initial topographic and bathymetric information which is replaced by more precise data wherever they are available. Bathymetric data is locally improved by ship measurements

and nautical charts. Topographic information is improved by the SRTM data set [25] which is freely available at a resolution of 90 m, however the vertical accuracy is usually not sufficient for model studies of runup in the coastal domain. In the area of Indonesia the SRTM data were additionally processed by the German Aerospace Agency (DLR) and provided at a resolution of 30m. In Aceh region additional bathymetric and topographic data were provided by BPPT Jogyakarta.

4.1.2. Source model

In tsunami modeling it turns out that the exact knowledge of the source, i.e. the initial conditions of the model is of crucial importance for comparisons with data. Usually the source parameters are optimized with respect to certain measurements and normally it's not possible to match model results with different measurements like tide gauges *and* inundation. The source model used in the following studies is based on the results presented in [26]. The objective of that paper is to optimize the subfaults of the earthquake such that an optimal agreement with certain tide gauge records is obtained. The resulting subfaults are shown in figure 7. In order to demonstrate the impact of source parameters with respect to the matching with data the orientation of the Southern faults is modified as indicated in that figure. The strike angle of subfaults A/C is changed from 340/340 degrees as proposed in [26] to 290/320 degrees. All other parameters can be found in in [23, 26].

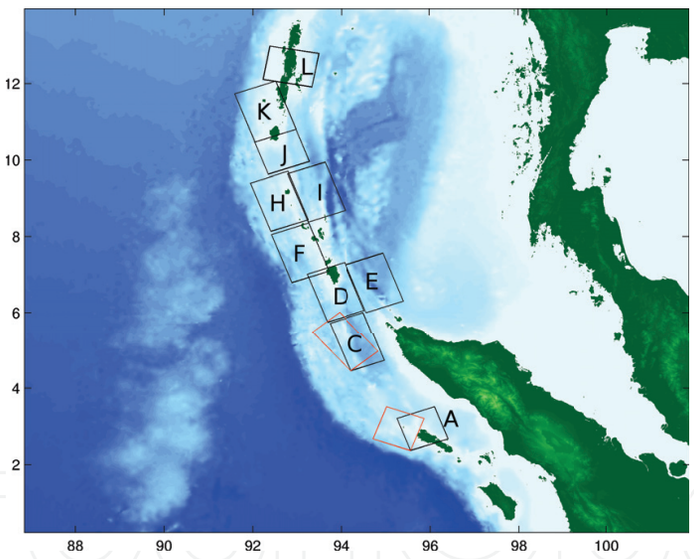


Figure 7. Sub-faults as proposed in [26]. The rupture area has been decomposed into 12 sub-regions. With a rupture speed of 1.7 km/s, the whole rupture process takes 12 min. Faults B and G have zero slip in our experiments and are not displayed. The red faults have different strike angle and show better agreement with satellite altimetry.

4.1.3. Model setup

The mesh used in these experiments consists of 5 million nodes and 10 million triangles. The finest resolution enforces a time step of half a second. The model is integrated for 10 hours. In the positions along the satellite tracks the model state is written to a file every second.

This enables a careful comparison between model and satellite altimetry data. Additional information on model setup and initialization is contained in [23].

4.1.4. Satellite altimetry

For the first time the Indian Ocean tsunami was observed by several Satellite missions. **Jason 1 (J1)** and **TOPEX/POSEIDON (T/P)** were above the bay of Bengal about two hours after the earthquake, whereas **ENVISAT** observed the tsunami about 3h20′ after the event. In all cases the tsunami signal was extracted from the altimeter measurements by subtracting the data from consecutive cycles. Table 1 summarizes the cycles that were taken into account in the three missions. Figure 8 contains the groundtracks of **J1** and **T/P** whereas figure 9 displays the extracted tsunami signal for **J1** and **T/P**. The model results are interpolated in time and space and extracted from a Hovmöller diagram as shown in figure 10. The **J1** signal in figure 9 shows clearly a double peak in the position of the leading wave crest which is due to the partial waves generated by the southern subfaults, whereas in the **T/P** measurements these partial waves overlap. This behavior is reproduced by the model however as it turns out the matching depends strongly on the fault parameters. Changing the strike angles in fault A from 340 to 290 and in fault C from 340 to 320 improves the matching and lowers the RMS errors as indicated in table 1.

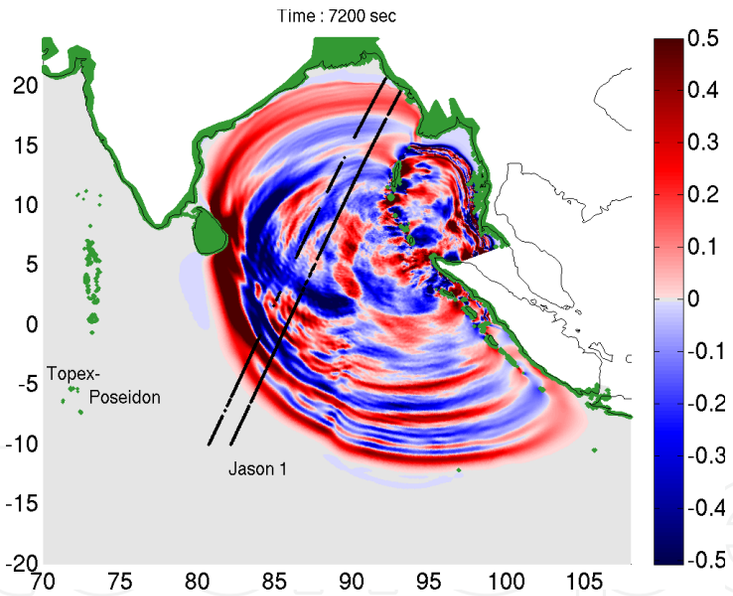


Figure 8. Model snapshot after two hours. Sea surface elevation together with the positions of the satellite tracks Jason 1 and TOPEX/POSEIDON

Mission	Pass	Cycle	Equator time	rms (340/340)	rms (290/320)
Jason 1	129	109	02:55 UTC	0.243 m	0.238 m
Topex/Poseidon	129	452	03:01 UTC	0.223 m	0.164 m

Table 1. Satellite Missions used in this study for data comparison. The last columns quantify the RMS error obtained in scenarios with different strike angles in subfaults A and C (figure 7).

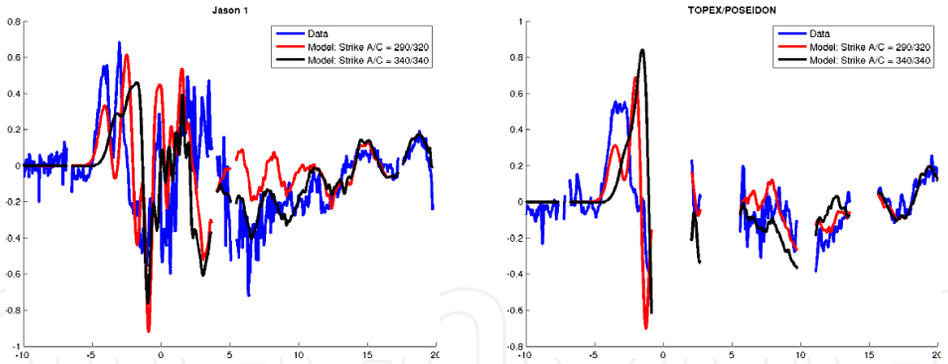


Figure 9. Tsunami signal extracted from satellite tracks Jason 1 and TOPEX/POSEIDON (blue lines) together with model results along the tracks interpolated in space and time (red and black lines).

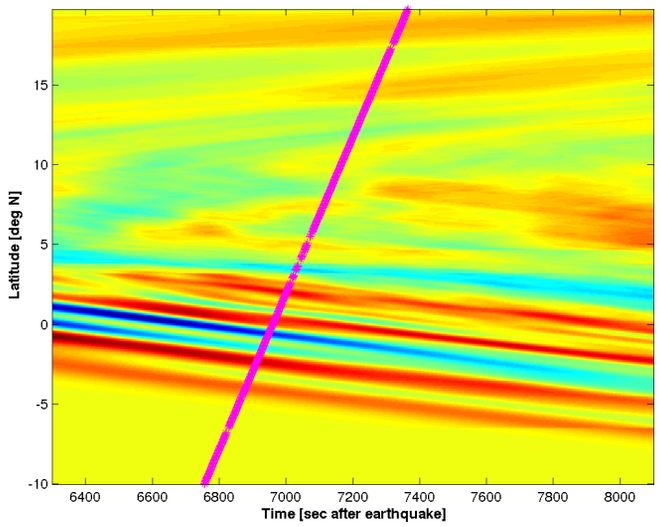


Figure 10. In the location of the satellite tracks (figure 8) the sea surface elevation is written to file every second. From the resulting Hovmöller diagram the model results corresponding to the satellite observations as shown in figure 9 are interpolated in space and time.

4.1.5. Inundation

After the event in December 2004 several field surveys examined the runup and flow depth in the affected regions. In the area of Banda Aceh, which was most heavily hit by the tsunami eight locations with well documented field measurements were chosen to compare model runup to these results. Runup and flow depth depend heavily on the prescribed roughness parameterization. Several experiments with identical initial conditions and varying Manning parameter were conducted. In all cases constant manning number was applied in the whole model domain.

Figure 11 shows the locations as well as a comparison of measurements and model results for different roughness parameters in a bar diagram. These results are obtained with strike angles 290/320 in subfaults A/C. From the corresponding rms errors the best fitting Manning number for experiments with constant parameters can be chosen. Figure 12 shows the flow depth in Aceh region together with a line depicting the boundary of inundation as it was obtained from Satellite images (provided by DLR).

Figure 13 displays the flow depth comparison for different strike angles in the Southern subfaults. Also in this respect the modified orientation improves the results considerably.

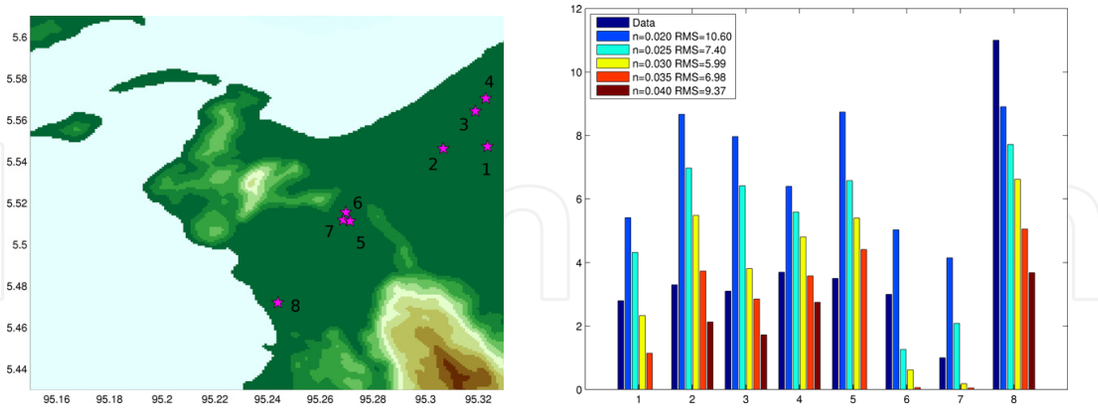


Figure 11. a) Positions of field measurements, b) model results for varying roughness parameters in comparison.

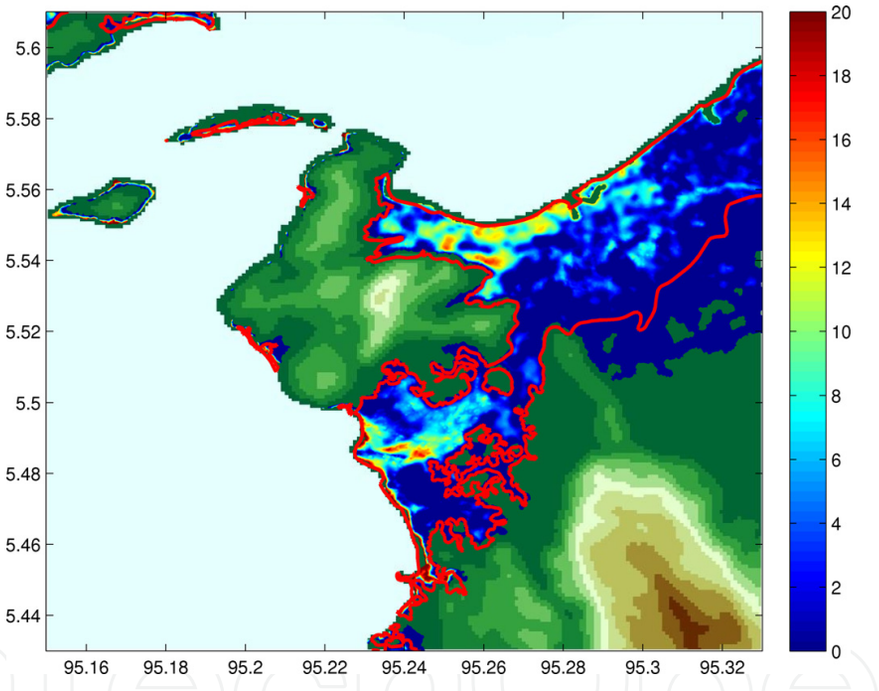


Figure 12. Flowdepth obtained for n=0.025 in Aceh region. The red line indicates the inundated area as it was determined from satellite images and provided by DLR.

4.1.6. Tide gauge records

The Indian Ocean tsunami was observed by tide gauges world wide. Since the arrival time and estimated wave height are among the most important warning products good matching between model results and arrival times and the height of the leading wave crest as they were recorded by tide gauges is desirable. Therefore hindcast experiments with such comparisons are included in the present study as well. Figure 14 summarizes the time series in some of the locations throughout the Indian Ocean where data is available. The comparisons between tide gauge records and model results show generally a good agreement with respect to arrival

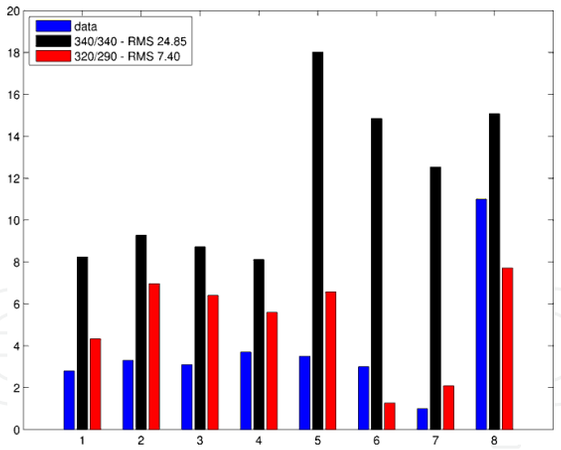


Figure 13. Flowdepth comparison for experiments with strike angles of plates A and C set to 340/340 and 290/320 (compare figure 7). The rms error is considerably improved by the adjustment.

time. The wave height of the leading crest is sometimes underestimated however in most of the locations the agreement is very good. The orientation of the Southern subfaults does not influence the results in far distance as Salalah and Lamu show, the matching in Colombo is slightly better with the uniform values (340/340). This is consistent with the derivation of these strike values as this station was used for optimization in [26].

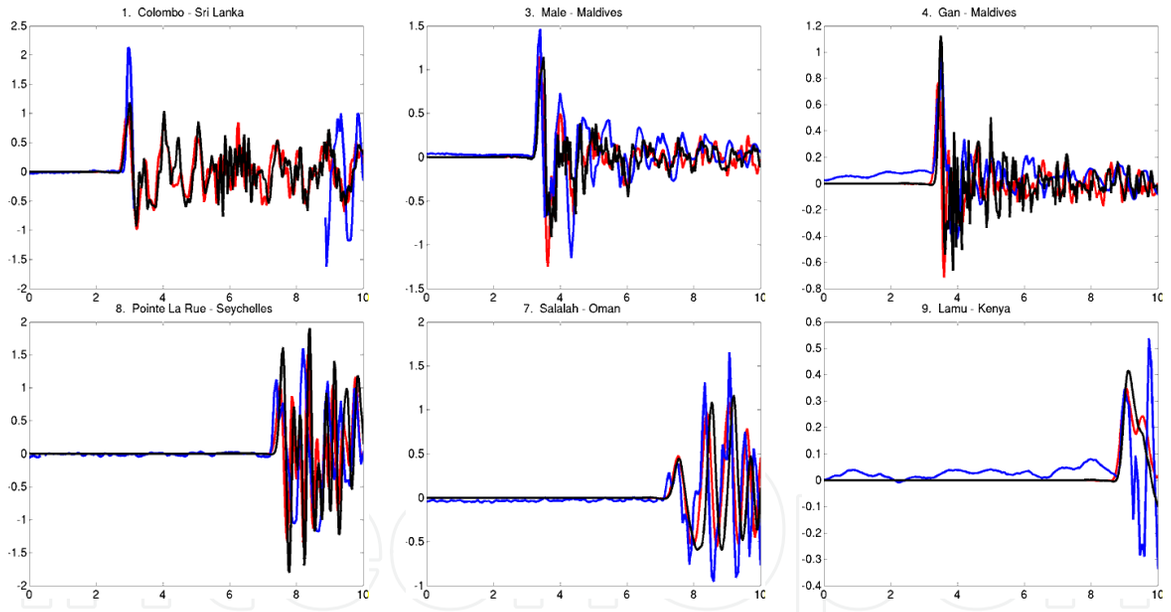


Figure 14. Tide gauge records (blue lines, time in hours, elevation in meter) and corresponding model results in locations displayed in figure 6. The red lines show results for strike angles 290/320 degrees, black lines the corresponding results for 340/340 degrees in subfaults A/C.

4.1.7. Summary of the Indian Ocean study

Summing up, it turns out that TsunAWI is able to reproduce observational results on several scales of wave propagation. Both the large scale propagation and arrival times throughout the Indian Ocean as well as the inundation in a selected area with high resolution is feasible in the approach with unstructured meshes. However the model results depend strongly on the quality of the source model.

4.2. Inundation experiments with high resolution

The scenarios generated for the tsunami database are based on a mesh with resolution ranging from 10 km in the deep ocean to 150 m along the global coastline and 50 m in priority regions. This resolution is certainly not high enough for detailed inundation simulations. Hazard maps are based on data sets with much higher resolution and the corresponding model setup must contain a comparable mesh. The shallow water equations are based on very small aspect ratio defined in (9) and as soon as the wave is determined by very fine scale topographic features the validity of the SWE becomes questionable. As long as the focus of such model studies is put on the inundated area alone the limitations of the SWE might still be acceptable and in the following experiments with high resolution are presented. The actual error however has to be investigated and comparisons to more appropriate models have to be performed. Section 2.5 deals with some of the improvements possible with nonhydrostatic corrections in idealized settings. Within the GITEWS project hazard maps were produced by DLR based on model

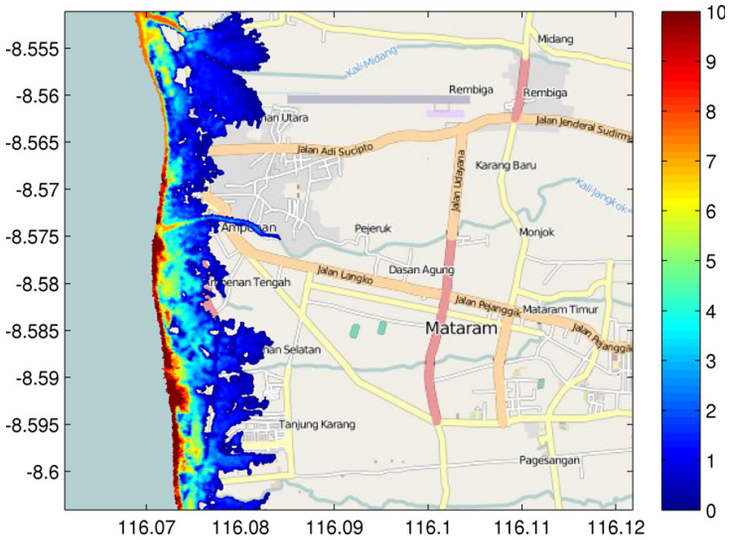


Figure 15. Inundation in Mataram. Flowdepth in the model study based on the Intermap DSM. The bottom roughness is given by a constant Manning value n=0.02.

results with MIKE 21 FM carried out by the German Research Center Geesthacht (GKSS). The Manning roughness parameter in these model runs are varying in space and given by detailed roughness maps. Details on this approach and the model can be found in [27] and citations therein.

The focus of this section is to highlight the importance of the bottom roughness parameter. Simulations of tsunamis with identical initial conditions were carried out in a mesh with resolution up to 5 m. The study area is Mataram, on the island of Lombok, Indonesia. The topography data in this case was based on the Intermap data set and provided by DLR. The resolution of the topography data is 5m and two versions, a digital surface map (DSM) and digital terrain map (DTM) were used. The DSM version is a first-reflection data set and contains elevations of vegetation and buildings. The DTM on the other hand is a model where all these features were removed.

Figure 15 displays the flow deph based on the DSM topography data, whereas figure 16 shows the same quantity for the DTM data with three different values of Manning's n. Additionally,

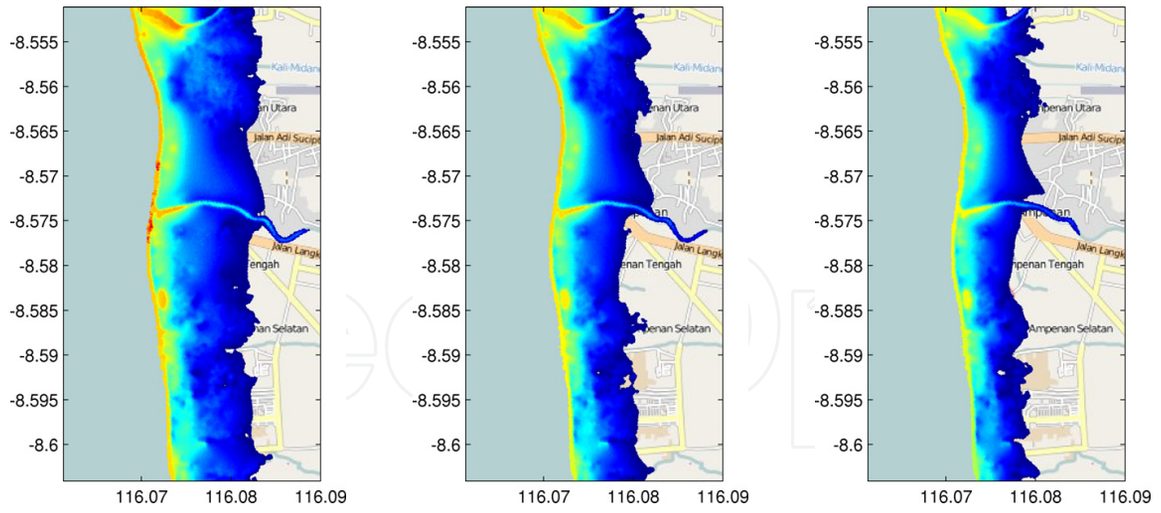


Figure 16. Results as in figure 15, however for Intermap DTM with three different Manning parameters n=0.04, n=0.06, and n=0.08 in the left, middle and right panel.

in case of a tsunami buildings and infrastructure will partly collapse and result in a very heterogenious fluid flow which may be only poorly approximated by a bottom friction parameterization. The result in figure 15 contains small scale features, however since it doesn't take into account the destruction of buildings and vegetation, it may be underestimating the true inundation. [27] suggests the use of DTM data with detailed roughness maps. Results for DTM data and different roughness values are displayed in figure 16. According to [27] the right panel corresponds rather to the situation of an urban area with partly collapsing buildings whereas the left panel corresponds to the situation of the whole area covered by coarse sand.

Given the vast differences displayed in figure 15 and 16 this section and its results is mostly meant to raise the awareness for the dependency of inundation results on the friction parameters. The quality of topography data plays an even bigger role and the best suited data set and model parameterization must be chosen before hazard maps are produced.

5. Tide-tsunami interaction

For investigating the influence of tidal motion on tsunami wave propagation three model runs were carried out: a) pure tidal motion, b) pure tsunami wave propagation and c) tsunami wave propagation on the background tidal motion. As object of modelling we have chosen the Indonesian coast including south part of Java, Bali, Lombok, Sumbawa and Sumba islands and North Sea. The choice of these two objects is not accidental. The first of these is the object with complex morphometry and sharp bathymetry, which contains a large number of islands and straits. The North Sea is a shelf sea with slowly varying bathymetry.

5.1. Interaction between tides and tsunami for Indonesian coast

For calculations, we use the ETOPO 30 sec. morphometry dataset and data on tides in the Indian Ocean derived from the TPXO6.2 dataset of oceanic tides [28]. The calculations were performed on an unstructured mesh (figure 17 a) with 177132 nodes and 347098 elements

with a time step of 20 s. The horizontal mesh size varies in the range between 160 m (in the inundation zone) and 29 km (deep ocean). The tsunami wave is initialized by a source model as used in the GITEWS scenario database (figure 17 b). The particular choice of the initial condition is irrelevant for our considerations here. The series of experiments deals with effects of nonlinear interaction between tidal waves and tsunamis in the Indian Ocean. A full solution (propagation of tsunami wave on the tidal background) and composite solution (an arithmetic sum of tsunami wave and tides computed separately) are compared. It turns out that the difference between these solutions is very significant (figure 18) reaching as high as 3.5 m in the coastal region (St.3) where nonlinearity is particularly important. It is noteworthy that the first tsunami wave is only slightly affected by nonlinearity (change in amplitude $\approx 5-8\%$, with max. amplitude of tsunami wave 16 m, St.3), while the second wave is affected more essentially, at $\approx$ 25% (with max. amplitude second tsunami wave 3.5 m). Also, the strong nonlinear interaction leads to phase changes.

In search of explanation as to why the impact of tide-tsunami interaction is so significant, we repeated the above cases once more but switching off the momentum advection term in the equation of motion. Figure 18 (Right panel) clearly shows that the evolution of potential and kinetic energy is now significantly different from the full nonlinear case. Hence we conclude that in the near-shore regime, non-linear interaction of the wave-induced velocities contributes greatly to the complex behaviour of tide-tsunami wave phenomena. The exact mechanisms still call for a more careful analysis and suggest a topic for future research.

5.2. Tide-tsunami interactions in the North Sea

The last known mega-tsunami to hit rim countries of the North Sea took place over 8,000 years ago. But coastal areas of the North Sea are vulnerable to tsunamis caused by localized underwater landslides. Numerical simulations are performed on the basis of a high-resolution multilayer model to study initial generation of waves by landslides in the Storegga area and with a TsunAWI model to study the wave propagation further in the North Sea.

As before, three simulations have been performed to identify the character of the nonlinear interaction of tide and tsunami waves. First simulation dealt with the M_2 tidal structure in the North Sea. In the second case only tsunami waves excited by a signal from the landslide model were simulated. The third simulation dealt with a joint solution for the tsunami wave on the

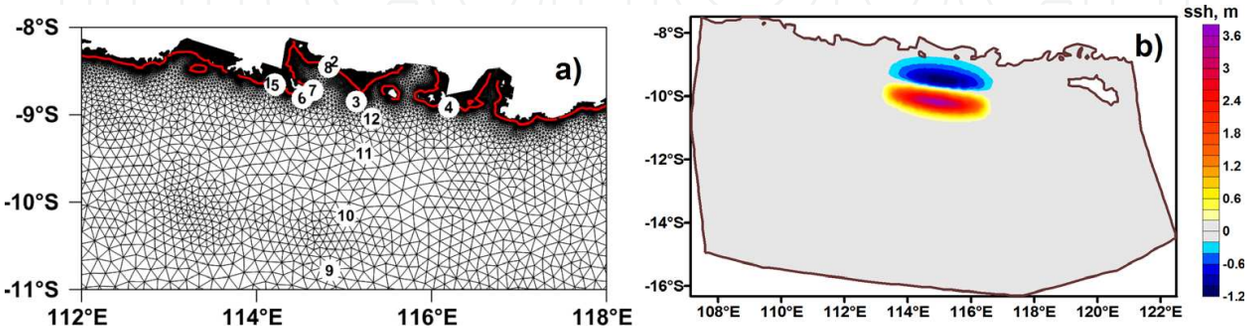


Figure 17. a) Part of the unstructured mesh with control stations. White curve marks coastal line. b) Initial condition for tsunami wave.

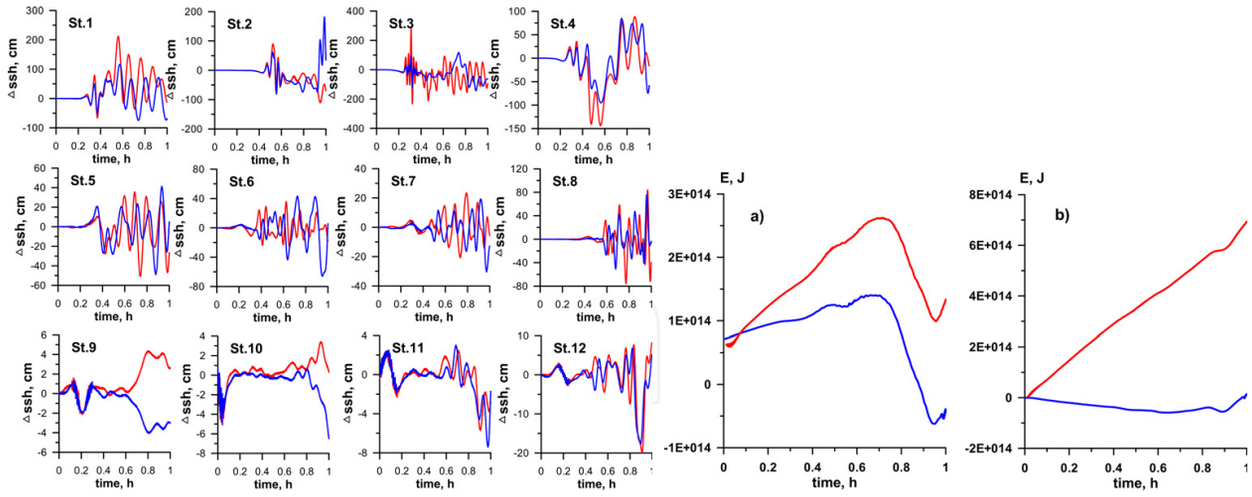


Figure 18. Left panel: Nonlinear interaction for control stations (1-4 - coastal; 5-8 - shelf; 9-12 - deep). Difference in elevation between full solution and composite solution. Red line - high tide; blue line - low tide. Right panel: Difference in potential (a) and kinetic energy (b) between full solution and composite solution. Red line - with advection in momentum equation; blue line - without advection.

background of semidiurnal tide. In this case the boundary information (north boundary) is represented by a superposition of two waves.

A combination of two Kelvin waves (one propagating from the northern open boundary along the coast of England and another through the English Channel) produces three nodal lines: on an output from English Channel, near north coast of Germany, and southern coast of Norway [11]. There is reasonable agreement for semidiurnal tidal elevations with respect to observation (figure 19).

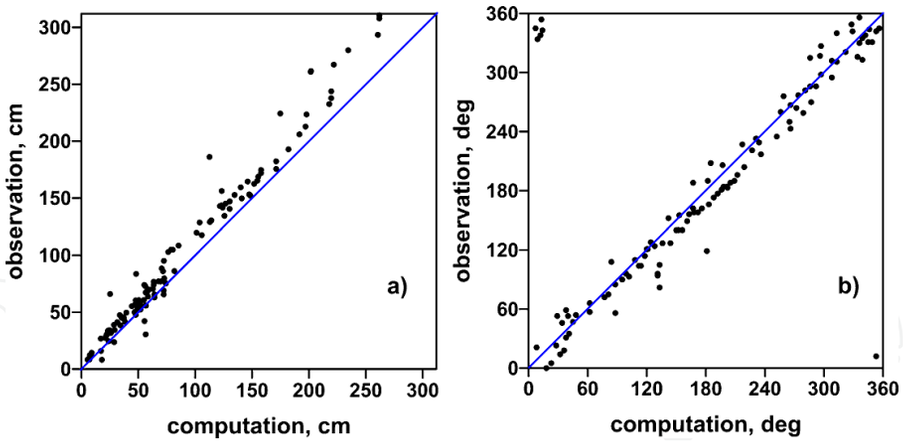


Figure 19. Correlation between the observed and computed values of the amplitudes (a) and phases (b) of the tide wave M_2. The RMS error of the computation is 29.8 cm (for 112 stations).

A two-layer model based on shallow water equations written in a curvilinear coordinate system is applied to simulate waves generated by hypothetical submarine slides at Storegga on the Norwegian continental slope (figure 20). The numerical method is based on composite schemes for split operators [29]. The model is initialized by prescribing submarine slides in the Storegga area off western Norway [30, 31]. The signal at the open boundary of the North Sea

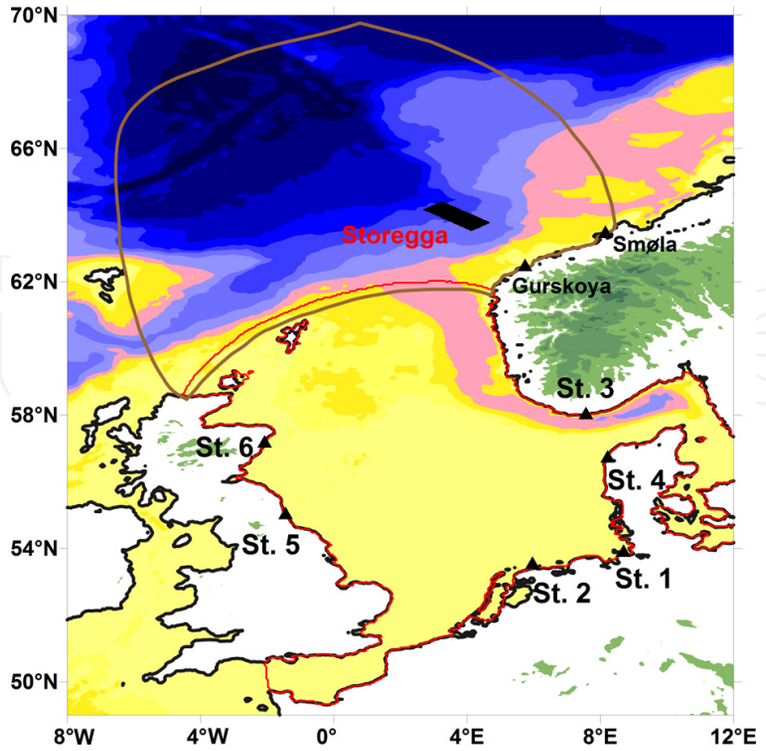


Figure 20. Computational domain with slide positions (Storegga) and control stations. The brown line shows the domain for submarine slides modelling. The red line marks the domain for tsunami wave propagation (TsunAWI model).

simulated by the model serves as the boundary condition for finite-element model (TsunAWI) used to simulate wave propagation further in the North Sea.

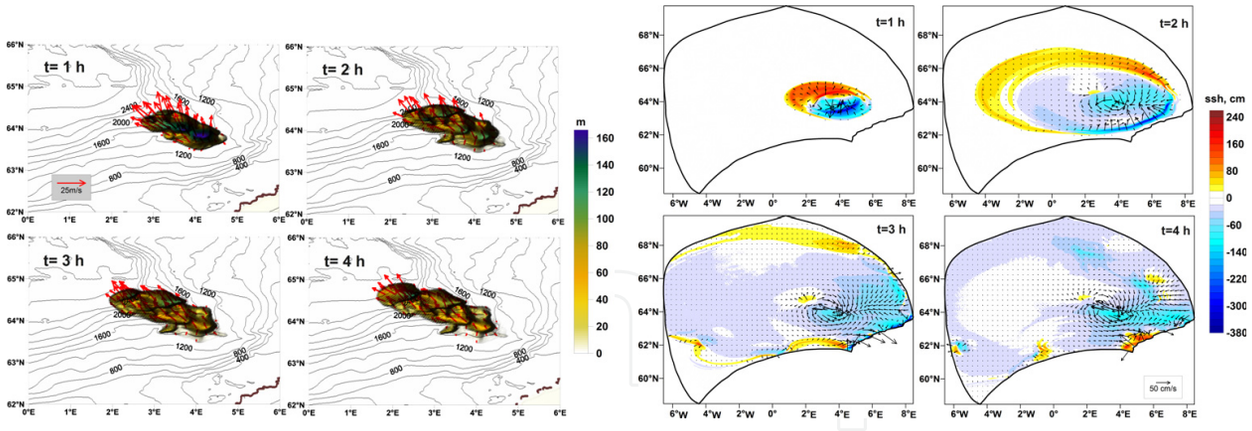


Figure 21. Thickness (m) and velocity (m/s) for Storegga landslide at four subsequent times (Left panel). Sea surface elevation (cm) and velocity (m/s) for Storegga landslide (Right panel) at four time instants.

Figure 21 (Left panel) shows the position, thickness of the submarine slide (Storegga) and velocity field in the bottom layer (landslide) at four different time moments. The slide velocity reaches 25 m/s, in agreement with [30, 31]. The submarine slide leads to long wave on the surface as shown in figure 21 (Right panel) for the same time moments as in figure 21 (Left panel).

A composite solution and full solution are compared. It turns out that the difference between these solutions is fairly large (figure 22, Left panel) reaching as high as 60 cm in the coastal region where nonlinearity is particularly important. Additional experiments showed that the arrival time of tsunami waves in the full solution varies but slightly. In search of explanation

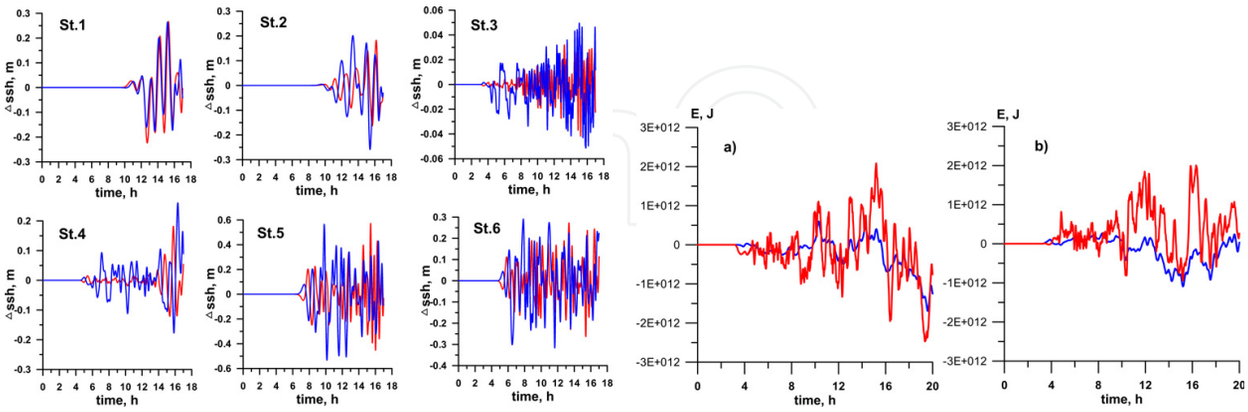


Figure 22. Left panel: Nonlinear interaction. Difference in elevation between a composite solution and full solution. Red line - high tide; blue line - low tide. Right panel: Difference in energy between a solution with advection and solution without (a) momentum advection (blue line) and solution without (b) nonlinearity in the continuity equation (red line).

as to why the impact of tide-tsunami interaction is so significant, we repeated the above cases once more but switching off the momentum advection term in the equation of motion (linear case) or nonlinearity due to change of layer thickness in the equation of continuity (figure 22, Right panel). Here we can see the other mechanism of tide-tsunami nonlinear interaction due to level change.

6. Validation of the nonhydrostatic approach

For comparison of the results delivered by the original shallow water model on the one hand with the nonhydrostatic extension on the other two standard testcases are carried out. The first one is investigated in [18], it describes the behavior of a standing wave within a closed basin in respect of the phase velocity depending on the ratio δ defined in (9). As second application a tank experiment (see [32]) is modeled and the results are compared against observation data at various instants. This example shows dispersive effects that occur when a solitary wave is running up a plane beach.

6.1. Standing wave in a basin

The computational domain Ω of this testcase presents a rectangular basin with fixed length and width $l = 10$ m and $w = 4$ m, respectively, while its depth h vary in different experiments between 0.25 m and 10.5 m. At the walls of the basin, condition (3) for solid boundaries $\partial\Omega_1$ is applied. With a wave length of $\lambda = 2l$ a standing wave with an amplitude of $a = 0.01$ m can be arranged by the initial condition

$$\zeta^0(x, y) = -a\cos(\frac{2\pi x}{\lambda}), \tag{18}$$

as illustrated in Figure 23 a). Both, horizontal and vertical velocity equal zero initially. In the absence of sinks and sources, two waves with same amplitude and frequency emerge. They move in opposite directions and form a standing wave with antinodes at the boundaries, $x \in \{0, l\}$, and a node in the middle of the basin, $x = l/2$. An unstructured mesh with a resolution of about 0.125 m covers the domain Ω. Using a time step size of $\Delta t = 0.005$ s, several experiments with varying basin depths were carried out with both the original shallow water model and the nonhydrostatically corrected one. Because of the periodicity, the propagation speed can be determined. In this example an inviscid fluid is assumed, so that the pressure gradient is the only force. Modifications of the pressure term due to nonhydrostatic effects entail changes of the motion. In Figure 23 b) the results of both models are compared with the reference propagation speed, estimated by

$$c = \sqrt{\frac{g}{k} \tanh{(kh)}}, \tag{19}$$

in which $k = 2\pi/\lambda$ is the wave number. If $\delta \ll 1$, the argument of the hyperbolic tangent in (19) is very small and the approximation $\tanh(x) \approx x$ can be adopted. So, the propagation speed converges to the phase velocity $c_{sw} = \sqrt{gh}$ that is independent of wavelength and characterizes motions in the standard shallow water approximation. It is not surprising that the phase velocity curve based on the shallow water model is congruent with c_{sw} for all δ. More interesting is the result of the nonhydrostatic approach: although it is simplified by using depth-averaged values, it offers a good approximation to the propagation speed up to ratio δ in excess of about 0.4. Consequently, as δ is increased, the nonhydrostatic correction provides a better approximation to the wave propagation speed.

6.2. Solitary wave on a plane beach

In the second testcase the results of the shallow water model and the nonhydrostatic approach are compared to observation data of a tank experiment [32]. The main part of tank is of constant water depth d. Near the shoreline ($x = 0$), the bathymetry gradually ascents with a constant slope of $\tan(\alpha) = 1/19.85$, as depicted in Figure 24. All spatial quantities in the

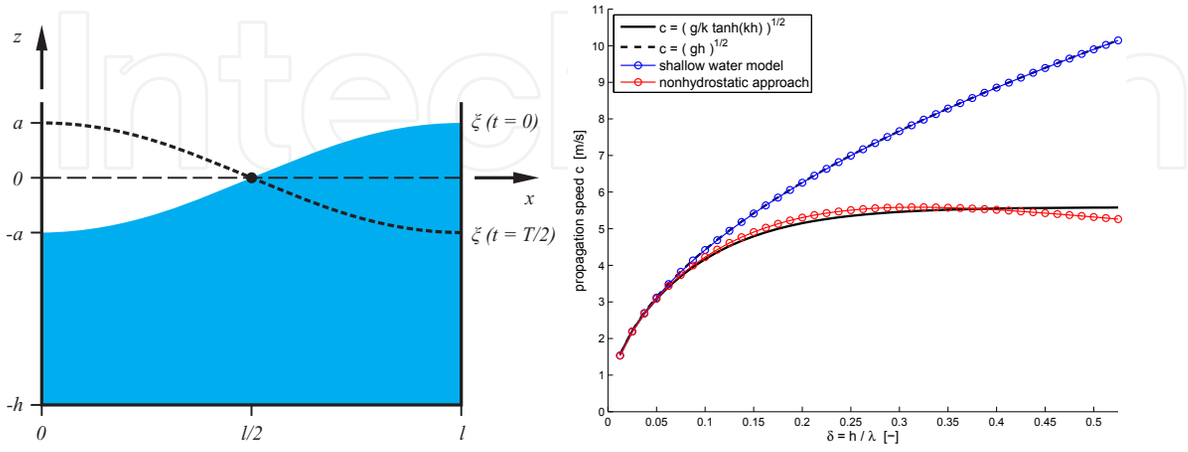


Figure 23. a) Setup of testcase 6.1: Standing wave in a basin. b) Different results in reference to propagation speed c.

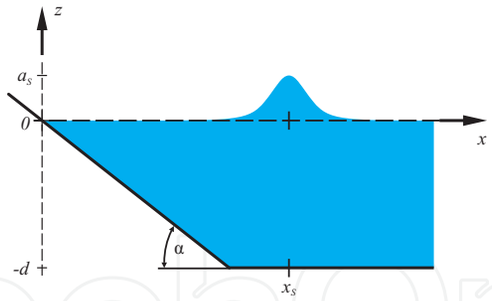


Figure 24. Setup of testcase 6.2: Solitary wave on a plane beach.

model setup are made dimensionless with the tank depth d. To simplify matters, $d = 1$ m is chosen. A solitary wave with maximum height $a_s := a/d$ is given by

$$\zeta^0(x,y) = \frac{a}{d}\text{sech}^2\left(\sqrt{\frac{3a}{4d}}(x - x_s)\right), \quad x_s = \frac{d}{\tan(\alpha)} + \sqrt{\frac{4d}{3a}}\text{arccosh}(\sqrt{20}). \tag{20}$$

with an initial horizontal velocity of $\mathbf{v}^0 = (-\zeta^0\sqrt{g/d}, 0)^T$. The vertical velocity is prescribed by the boundary conditions (13) and (14). While the ramp can be flooded for $x < 0$, boundary condition (3) on $\partial\Omega_1$ are imposed at the solid walls of the tank. An unstructured mesh with $\Delta x \in [0.1, 0.2]$, in which the finer resolution accords to the ascending part, covers the computational domain $\Omega = [-10, 70] \times [-0.5, 0.5]$. The time step is selected as $\Delta\tau = \Delta t\sqrt{g/d} = 0.004$. With the help of a Manning factor of $n = 0.01$ the low friction inside of the tank is approximated. By setting the maximum wave height $a_s = 0.0185$, the shallow water model and the nonhydrostatic approach provide similar results which agree very well with the observation data. More interesting is the case of breaking wave with $a_s = 0.3$. Figure 25 illustrates different stages of the flow evolution in four snapshots. It is apparent that the nonhydrostatic approach approximates the shape of the solitary wave much better than

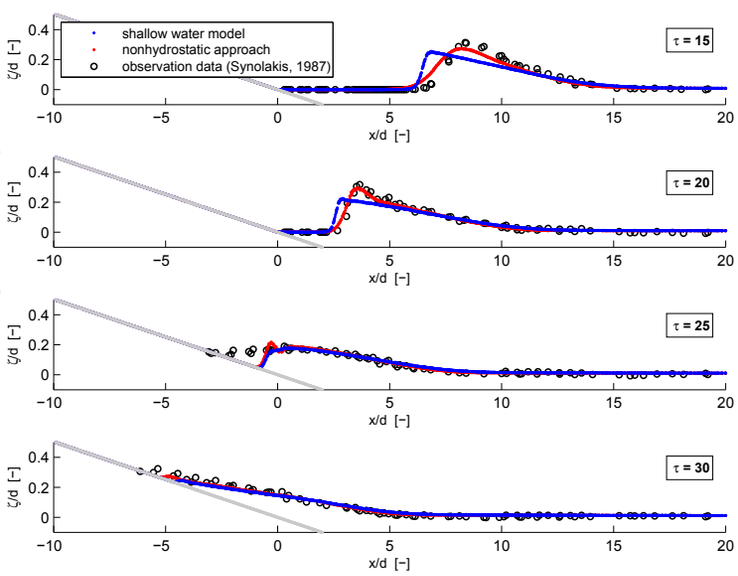


Figure 25. Snapshots at different times $\tau = t\sqrt{g/d}$ for a solitary wave with a maximum wave height of $a_s = a/d = 0.3$.

the hydrostatic shallow water model. As a consequence of boundary condition (13) the wave front experiences a vertical displacement. Since this dispersive process cannot be represented by the shallow water model, its wave front steepens in an unnatural way. Furthermore, the snapshot at $\tau = 30$ shows clearly that there are some differences with respect to inundation, which is very important as concerns tsunami warning.

7. Discussion

The combination of non-conforming velocity with linear elevation suggests a well-rounded choice for shallow-water modelling on unstructured triangular grids, with a particular focus on simulating tsunami wave propagation. Although our approach was initially inspired by the algorithm proposed by Hanert et al. [10] the resulting model is essentially different from it in a number of key directions. First, it is equipped with wetting and drying algorithms and can simulate inundation caused by tsunami. Second, it suggests a choice of stably working discretization of the momentum advection which all improve over the original method of Hanert et al. [10] and differ between themselves in a degree of smoothing applied. Third, it uses the Smagorinsky horizontal viscosity which is crucial for keeping the dissipation on the level that does not affect the quality of the solution. Finally, the explicit time stepping and use of the nodal quadrature (mass matrix lumping) of the time derivative term in the continuity equation ensure numerically efficient performance while providing a straightforward and easy to implement algorithm.

Nonhydrostatic effects become important when vertical acceleration is not negligible. For tsunami wave generation and propagation it can happen at the very initial stage and during run up. In this context, we present an algorithm of the nonhydrostatical pressure for vertical averaged equations.

We introduced the architecture of the German-Indonesian Tsunami Early Warning System (GITEWS) and methodology for the GITEWS multi-sensor selection. The selection algorithm uses a multi sensor approach combining the different available sensor types (SeisComP3, CGPS and Tide Gauges) to acquire a set of best matching pre calculated scenarios (Tsunami Scenario Repository, TSR) to an earthquake event. The basic principle is to reduce the number of possible tsunami scenarios by using independent measurements of the same event. Only a small number of scenarios can match the independent measurements, even with high uncertainty in each individual set of measurements, since the combination needs to fit.

One of the important stages of the successful use of the numerical model is its verification and validation. This work has been performed on test cases and published in [33].

We simulated the tsunami event generated by the Sumatra-Andaman (2004) and Tōhoku (2012) earthquakes. The model results were compared to available data (tide gauge, satellite altimetry, and field measurements in the inundation area). Given still only approximately known parameters of the tsunami source the coincidence between the model and observation is indeed good. Not only the arrival time of the first wave is reliably simulated, but the entire shape of the signal is reproduced reasonably well, and with correct amplitude. The model can be considered as an easy to use and reliable tool which not only serves the purposes of

GITEWS but can be employed for other tasks which can be described in the framework of shallow water equations (with exception of true shock waves for which continuous elevation is a suboptimal choice).

Simulations suggest strong nonlinear interaction between the tsunami and tidal waves. The major difference between tsunami simulations with and without tides occurs in the run-up region. Two mechanism of nonlinear interaction were found to be directly related to the morphometry of the object. In areas with high variability in morphometry (sharp bathymetry, complex coastline, etc.), the main role is played by the nonlinear interaction of tidal velocities and tsunamis velocity. Another mechanism of nonlinear interaction operates through the changes in the thickness of the water layer in the presence of tides, which is typical for shallow areas. In this case besides the amplitude of the incoming wave, the arrival time can vary due to the change in wave phase speed. These results lead us to conclude that the account of tidal dynamics may prove to be necessary for the faithful modelling of tsunami waves.

For comparison of the results delivered by the shallow water model in the original state and with the nonhydrostatic extension on the other two standard test cases are executed. This example shows dispersive effects that occur when a solution is running up a plain beach.

The comparison between the results of the original shallow water model and the model with the nonhydrostatic correction, two test cases were performed. They illustrate the importance of dispersive effects, which may have implication to inundation prediction. The inclusion of nonhydrostatic effects may therefore be necessary for successful modeling of tsunami wave propagation.

Brief overview

The wave propagation model TsunAWI based on finite elements was presented. We also introduced the architecture of the Tsunami Early Warnin System and methodology for the multi-sensor selection. We simulated the tsunami events generated by the Sumatra-Andaman (2004) and Tōhoku (2012) earthquakes. Part of our work addresses the influence of tidal dynamics on tsunami wave propagation in coastal areas. The impact of nonhydrostatic effects is investigated in this study.

Acknowledgements

TsunAWI is the result of joint developments of different groups within AWI namely the computing center and the climate dynamics section. We acknowledge Jörn Behrens, Dmitry Sein, and Dmitry Sidorenko for contributions to the model development. We acknowledge Ralf Kiefl from the German Aerospace Agency (DLR) for providung us with inundation areas estimated from satellite images and NOAA/PMEL/NOAA Center for Tsunami Research for providing satellite altimetry data. We acknowledge Widjo Kongko for providing us with field measurements in Aceh region. The tide gauge data were provided by the Survey of India and National Institute of Oceanography and by the University of Hawaii Sea level Center within the Global Sea Level Observing System (GLOSS-IOC). Matthias Mück from DLR provided us with the Intermap DTM and DSM topography data in Mataram.

Author details

Alexey Androsov, Sven Harig, Annika Fuchs, Antonia Immerz, Natalja Rakowsky, Wolfgang Hiller and Sergey Danilov
Alfred Wegener Institute for Polar and Marine Research, POB 120161, 27515 Bremerhaven, Germany

8. References

[1] Kienle J, Kowalik Z, Murty T. S (1987) Tsunamis generated by eruptions from Mount St.Augustine Volcano, Alaska. Science, 236, 1442–1447.
[2] Greenberg D. A, Murty T, Ruffman A (1987) A numerical model for Halifax Harbor tsunami due to the 1917 explosion. Marine Geodesy, 16, 153–167.
[3] Baptista A, Priest G, Murty T (1993) Field survey of the 1992 Nicaragua Tsunami. Marine Geodesy, 16, 1692–1703.
[4] Mofjeld H, Gonzales F, Titov V, Venturato A, Newman J (2007) Effects of tides on maximum tsunami wave heights: probability distributions. Journal of Atmospheric and Oceanic Technology, 24, 117–123.
[5] Weisz R, Winter C (2005) Tsunami, tides and run-up: a numerical study. Papadopoulos G. A Satake K (eds.), Proceedings of the International Tsunami Symposium, Chania, Greece, 27-29 June 2005.
[6] Kowalik Z, Proshutinsky T, Proshutinsky A (2006) Tide-tsunami interactions. Science of Tsunami Hazards, 24, 242–256.
[7] Titov V. V, Synolakis C. E (1995) Evolution and Runup of Breaking and Nonbreaking waves using VTSC-2. Journal of Waterway, Port, Coastal and Ocean Engineering, ASCE, 121, 308–325.
[8] Oliger J, Sundström A (1978) Theoretical and practical aspects of some initial boundary value problems in fluid dynamics. SIAM J. Appl. Math., 35, 419–446.
[9] Androsov A, Klevanny K, Salusti E, Voltzinger N (1995) Open boundary conditions for horizontal 2-d curvilinear-grid long-wave dynamics of a strait. Adv. Water Resour., 18, 267–276.
[10] Hanert E, Le Roux D, Legat V, Deleersnijder E (2005) An efficient Eulerian finite element method for the shallow water equations. Ocean Modelling, 10, 115–136.
[11] Maßmann S, Androsov A, Danilov S (2008) Intercomparison between finite element and finite volume approaches to model North Sea tides. Continental Shelf Research, 30, 680–691.
[12] Lynett P, Wu T.-R, Liu P.-F (2002) Modeling wave runup with depth-integrated equations. Coastal Engineering, 46, 89–107.
[13] Smagorinsky J (1963) General circulation experiments with the primitive equations. Mon. Wea. Rev., 91, 99–164.
[14] Shewchuk J (2006) Triangle: engineering a 2d quality mesh generator and Delaunay triangulator. manocha D. (ed.). In: Lin MC, Applied computational geometry: towards geometric engineering, pp. 203–222, Springer, Heidelberg.
[15] Frey W, Field D (1991) Mesh relaxation: a new technique for improving triangulations. Int. J. Numer. Methods Eng., 31, 1121–1133.

[16] Casulli V (1999) A semi-implicit finite difference method for non-hydrostatic, free-surface flows. International Journal for Numerical Methods in Fluids, 30, 425–440.
[17] Cheung K. F, Yamazaki Y, Kowalik Z (2009) Depth-integrated, non-hydrostatic model for wave breaking and run-up. International Journal for Numerical Methods in Fluids, 61, 473–497.
[18] Walters R. A (2005) A semi-implicit finite element model for non-hydrostatic (dispersive) surface waves. International Journal for Numerical Methods in Fluids, 49, 721–737.
[19] Fleischer J, Häner R, Herrnkind S, Kloth A, Kriegel U, Schwarting H, Wächter J (2010) An integration platform for heterogeneous sensor systems in GITEWS - Tsunami Service Bus. Natural Hazards and Earth System Science, 10, 1239–1252.
[20] Steinmetz T, Raape U, Teßmann S, Strobl C, Friedemann M, Kukofka T, Riedlinger T, Mikusch E, Dech S (2010) Tsunami early warning and decision support. Natural Hazards and Earth System Science, 10, 1839–1850.
[21] Behrens J, Androsov A, Babeyko A. Y, Harig S, Klaschka F, Mentrup L (2010) A new multi-sensor approach to simulation assisted tsunami early warning. Natural Hazards and Earth System Science, 10, 1085–1100.
[22] Babeyko A, Hoechner A, Sobolev S. V (2008) Modelling tsunami generation for local tsunami early warning in Indonesia. Geophysical Research Abstracts, 10, eGU2008-A-01523.
[23] Harig S, Chaeroni C, Pranowo W. S, Behrens J (2008) Tsunami simulations on several scales: Comparison of approaches with unstructured meshes and nested grids. Ocean Dynamics, 58, 429–440.
[24] The general bathymetric chart of the oceans (GEBCO).
Webpage (http://www.gebco.net).
[25] Shuttle radar topography mission X-SAR / SRTM.
Webpage (http://www.dlr.de/srtm/).
[26] Tanioka Y, Yudhicara, Kususose T, Kathiroli S, Nishimura Y, Iwasaki S.-I, Satake K (2006) Rupture process of the 2004 great Sumatra-Andaman earthquake estimated from tsunami waveforms. Earth Planets Space, 58, 203–209.
[27] Gayer G, Leschka S, Nöhren I, Larsen O, Günther H (2010) Tsunami inundation modelling based on detailed roughness maps of densely populated areas. Natural Hazards and Earth System Sciences, 10, 1679–1687.
[28] Egbert G S E (2002) Efficient inverse modeling of barotropic ocean tides. Journal of Atmospheric and Oceanic Technology, 19, 183–204.
[29] Androsov A, Voltzinger N (2005) The Straits of World ocean - the general approach to modeling. Nauka, 188 pages, in russian.
[30] Harbitz C (1992) Model simulations of tsunamis generated by the Storegga Slide. Marine Geology, 105, 1–21.
[31] Løvholt F, Harbitz C, Haugen K. B (2005) A parametric study of tsunamis generated by submarine slides in the Ormen Lange/Storegga area off western Norway. Marine and Petroleum Geology, 22, 219–231.
[32] Synolakis C. E, Bernard E. N, Titov V. V, Kânoğlu U, González F. I (2007) Standards, criteria, and procedures for NOAA evaluation of tsunami numerical models. NOAA

Tech. Memo. OAR PMEL-135, NOAA/Pacific Marine Environmental Laboratory, Seattle.

[33] Androsov A, Harig S, Behrens J, Schröter J, Danilov S (2008) Tsunami modelling on unstructured grids: Verification and validation. Proceedings of the International Conference on Tsunami Warning (ICTW), Bali, Indonesia.

IntechOpen

IntechOpen